November 2021 • Volume 87 • Number 22

AEM

Applied and Environmental Microbiology

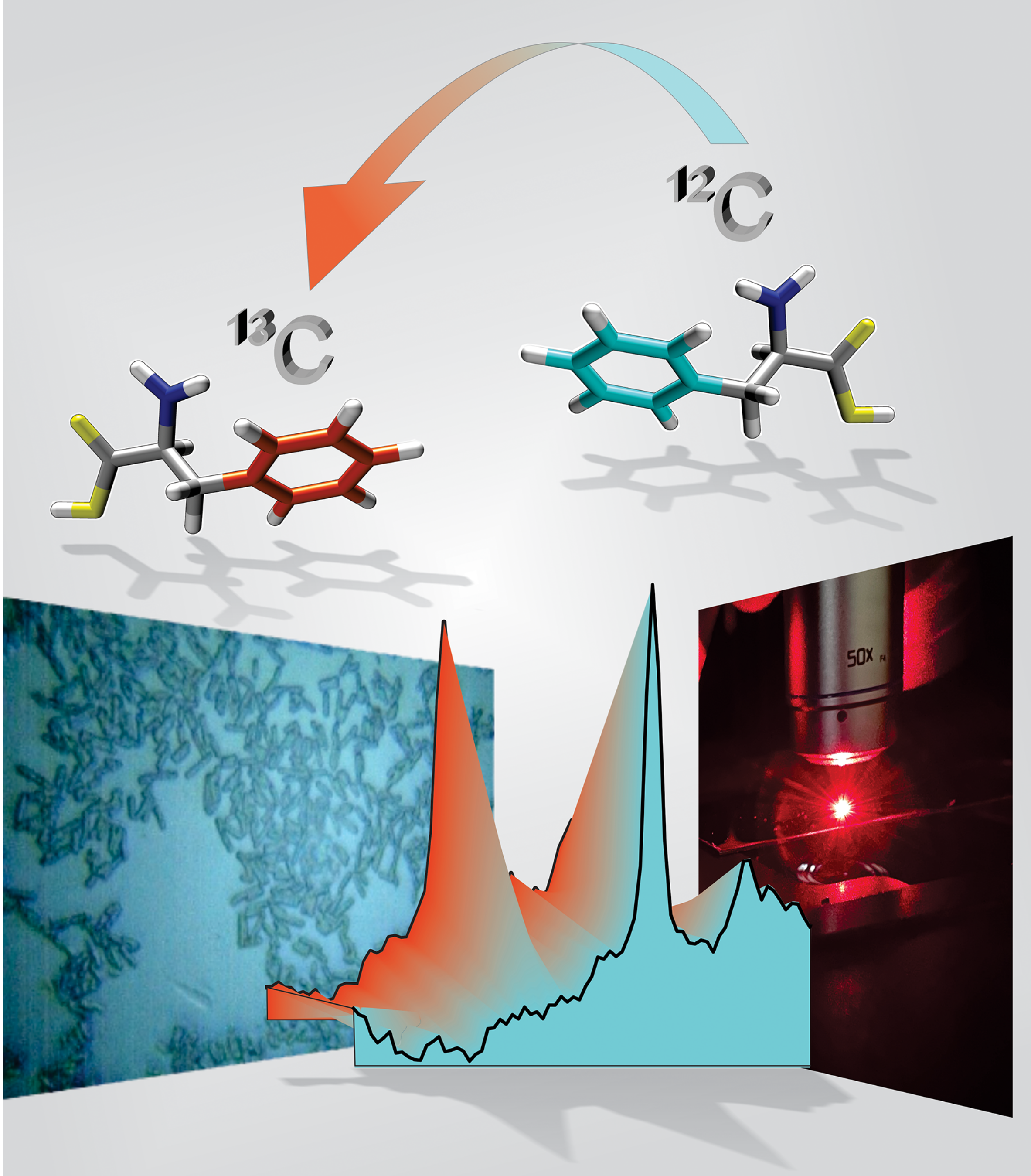

published twice monthly by

AMERICAN
SOCIETY FOR
MICROBIOLOGY

Cover Photograph: Laser Raman microspectrophotometer serving as a single-cell mass spectrometer. Montage showing a reflected bright-field micrograph (left) of a bacterial population being interrogated by a laser Raman microspectrophotometer (right) to measure ^{13}C-assimilation into their proteins from the media. “Red shifts” in spectral peaks to lower frequencies (lower center) reveal degree of ^{13}C-enrichment in the essential amino acid phenylalanine (structures above). In time course experiments using stable isotope probing (SIP) and Raman microspectrophotometric detection of ^{13}C-enrichment in individual bacteria, microbial growth rates are accurately calculated at both single-cell and population levels. (*See related article at e01460-21.*) (Graphics by T. Zaliznyak)

AMERICAN SOCIETY FOR MICROBIOLOGY | Applied and Environmental Microbiology®

METHODS

Using Stable Isotope Probing and Raman Microspectroscopy To Measure Growth Rates of Heterotrophic Bacteria

Felix Weber,[a] **Tatiana Zaliznyak,**[a] **Virginia P. Edgcomb,**[b] **Gordon T. Taylor**[a]

[a]School of Marine and Atmospheric Sciences, Stony Brook University, Stony Brook, New York, USA
[b]Department of Geology and Geophysics, Woods Hole Oceanographic Institution, Woods Hole, Massachusetts, USA

ABSTRACT The suitability of stable isotope probing (SIP) and Raman microspectroscopy to measure growth rates of heterotrophic bacteria at the single-cell level was evaluated. Label assimilation into *Escherichia coli* biomass during growth on a complex ^{13}C-labeled carbon source was monitored in time course experiments. ^{13}C incorporation into various biomolecules was measured by spectral "red shifts" of Raman-scattered emissions. The ^{13}C- and ^{12}C-isotopologues of the amino acid phenylalanine (Phe) proved to be quantitatively accurate reporter molecules of cellular isotopic fractional abundances (f_{cell}). Values of f_{cell} determined by Raman microspectroscopy and independently by isotope ratio mass spectrometry (IRMS) over a range of isotopic enrichments were statistically indistinguishable. Progressive labeling of Phe in *E. coli* cells among a range of ^{13}C/^{12}C organic substrate admixtures occurred predictably through time. The relative isotopologue abundances of Phe determined by Raman spectral analysis enabled the accurate calculation of bacterial growth rates as confirmed independently by optical density (OD) measurements. The results demonstrate that combining SIP and Raman microspectroscopy can be a powerful tool for studying bacterial growth at the single-cell level on defined or complex organic ^{13}C carbon sources, even in mixed microbial assemblages.

IMPORTANCE Population growth dynamics and individual cell growth rates are the ultimate expressions of a microorganism's fitness under its environmental conditions, whether natural or engineered. Natural habitats and many industrial settings harbor complex microbial assemblages. Their heterogeneity in growth responses to existing and changing conditions is often difficult to grasp by standard methodologies. In this proof-of-concept study, we tested whether Raman microspectroscopy can reliably quantify the assimilation of isotopically labeled nutrients into *E. coli* cells and enable the determination of individual growth rates among heterotrophic bacteria. Raman-derived growth rate estimates were statistically indistinguishable from those derived by standard optical density measurements of the same cultures. Raman microspectroscopy can also be combined with methods for phylogenetic identification. We report the development of Raman-based techniques that enable researchers to directly link genetic identity to functional traits and rate measurements of single cells within mixed microbial assemblages, currently a major technical challenge in microbiological research.

KEYWORDS Raman microspectroscopy, stable isotope probing, mass spectrometry, phenylalanine, cell growth rate, single-cell analysis, *Escherichia coli*

Assessing the activity and growth rates of microorganisms is central to our understanding of microbial community dynamics, the contributions of particular taxa to elemental fluxes, and a myriad of biogeochemical processes in the environment. Historically, a variety of techniques, such as cell counts, ATP dynamics, and the incorporation of radiolabeled compounds ([^{3}H]leucine and [^{3}H]thymidine), have been applied to estimate bulk community production and growth rates (1, 2). However, few studies have examined the *in situ* growth rates of specific taxa in mixed microbial

Citation Weber F, Zaliznyak T, Edgcomb VP, Taylor GT. 2021. Using stable isotope probing and Raman microspectroscopy to measure growth rates of heterotrophic bacteria. Appl Environ Microbiol 87:e01460-21. https://doi.org/10.1128/AEM.01460-21.

Editor Hideaki Nojiri, University of Tokyo

Address correspondence to Gordon T. Taylor, gordon.taylor@stonybrook.edu.

Received 27 July 2021
Accepted 28 August 2021
Accepted manuscript posted online 8 September 2021
Published 28 October 2021

assemblages, a necessity for evaluating the impact of individual phylotypes on ecological processes and elemental cycling (3).

Molecular approaches including analyses of rRNA content or rRNA/rRNA gene ratios have been used to estimate the growth rates of individual bacterial and archaeal taxa. These methods are often hampered by cell-to-cell variations in rRNA gene and rRNA copy numbers, thereby yielding loosely constrained growth estimates (3, 4). Recently developed metagenomic growth estimators, such as codon usage bias and the "peak-to-trough ratio," seem to predict growth rates of marine bacterial assemblages with only moderate success (5). Combining microautoradiography with fluorescence *in situ* hybridization (MAR-FISH) enables the detection of the assimilation of radiolabeled tracers (e.g., ^{3}H- and ^{14}C-substrates) into individual microbial taxa (6). MAR-FISH has been used extensively to assess the abundances of specific taxa that actively assimilate a tracer, but this method has rarely been used to estimate microbial assimilation rates (7, 8). Other single-cell techniques that can be combined with FISH, i.e., nanoscale secondary ion mass spectrometry (NanoSIMS) and Raman microspectroscopy, enable quantitative tracing of the assimilation of stable isotope-labeled substrates into cellular biomass (9–11). Being a nondestructive analysis, Raman microspectroscopy can also be combined with microfluidics to sort active cells and construct genetic libraries from recovered cells (12, 13). Raman-active sorting offers the possibility of higher phylogenetic resolution than microautoradiography or NanoSIMS methods, in which FISH probe selection limits taxonomic resolution. Stable isotope probing combined with NanoSIMS (SIP-NanoSIMS) is increasingly used to measure single-cell assimilation and growth rates (e.g., see references 14 and 15). The potential for deriving microbial assimilation and growth rates by combining SIP and Raman microspectroscopy (SIP-Raman) has not yet been fully explored.

Raman spectroscopy measures inelastically scattered photons emanating from a sample excited by laser light. The Raman scattering effect varies with the vibrational energy levels of the excited chemical bonds and thereby provides a molecular fingerprint. The ability to characterize the molecular composition of complex materials through the rapid, label-free, and nondestructive acquisition of spectra at high spatial resolution and with modest sample preparation requirements is a clear advantage of Raman spectroscopy over NanoSIMS (9, 16, 17).

Recently, the application of Raman-based approaches in the life sciences has significantly expanded. Raman spectral peak positions (measured in wavenumbers [cm^{-1}]) and intensities are indicative of an array of biomolecules (e.g., nucleic acids, proteins, lipids, chlorophyll, carotenoids, polyhydroxybutyrate, starch, and polyphosphate) and their abundances. Raman biomarkers enable molecular imaging of cells for the comprehensive examination of physiological and metabolic processes in cellular and microbiological studies (17–21). For example, molecular imaging by Raman microspectroscopy enabled the tracking of compositional changes and subcellular movements of DNA, protein, and lipid pools during cell division of HeLa cells and during viral infection of the cosmopolitan microalga *Emiliania huxleyi* (18, 22).

The assimilation of stable isotope-labeled substrates elicits useful shifts in a cell's Raman spectral profile. Raman spectral peaks of isotopically heavy biomolecules shift to lower wavenumbers than light isotopologues ("red shifted") because the increased atomic mass decreases the vibrational frequencies of excited chemical bonds (23). Unlike most other SIP techniques, including those used with NanoSIMS, SIP-Raman nondestructively detects label incorporation into biomolecular pools and does not require extraction or separation of heavy and light fractions of nucleic acids, proteins, or lipids for further analysis. Most SIP-Raman studies use ^{2}H-, ^{13}C-, and ^{15}N-labeled nutrients or ^{2}H in the form of D_2O to track these elements' movement from dissolved pools into individual cellular reporter molecules (9, 24). Huang et al. (23) were among the first to demonstrate [^{13}C]glucose assimilation in individual heterotrophic bacteria by means of wavenumber shifts in Raman spectral peaks assignable to carbohydrates, proteins, nucleic acids, and individual amino acids. Other ^{13}C- and ^{15}N-labeled substrates employed in SIP experiments include galactose, fructose, naphthalene, bicarbonate, and ammonium, and their incorporation was detected in

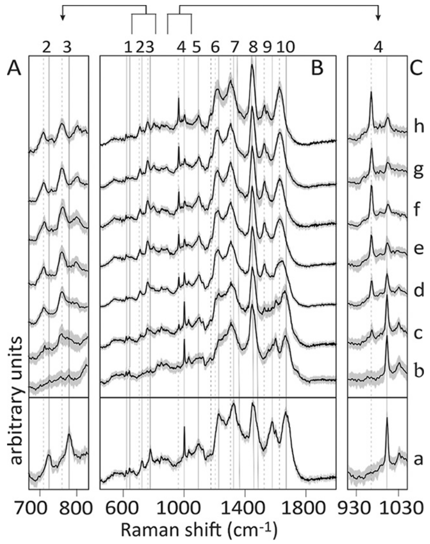

FIG 1 (B) Stacked Raman spectra of *E. coli* Bs-1 illustrating peaks emanating from macromolecules and their respective red shifts due to ^{13}C enrichment during the time course experiment. (A and C) Amplified views of original and red-shifted DNA and Phe peaks, respectively. Lines and shaded areas represent the averages and standard deviations computed at every wavenumber from 30 to 40 spectra obtained from individual cells. Peaks 1 to 10 (top) correspond to wavenumber assignments of vibrational modes in Table 1. (a) Composite spectrum of cells grown for 59 min at natural isotopic abundances. (b to h) Composite spectra acquired from cells grown in the most isotopically enriched media (f_{media} = 0.985), with incubation times and Raman-derived f_{cell} values as follows: 0 min and f_{cell} of 0.02 (b), 30 min and f_{cell} of 0.19 (c), 59 min and f_{cell} of 0.49 (d), 88 min and f_{cell} of 0.68 (e), 119 min and f_{cell} of 0.84 (f), 180 min and f_{cell} of 0.89 (g), and 270 min and f_{cell} of 0.93 (h).

multiple macromolecules within bacteria or accessory pigments of photosynthetic organisms (11, 25–28).

Several recent reviews highlight that SIP-Raman and "omics" approaches represent promising paths toward a deeper mechanistic understanding of microbial ecology because these tools can capture genetic identity, function, and process rates of key microbial community members *in situ* (24, 29, 30). Quantitative isotopic labeling of heterotrophic and photoautotrophic cells has been demonstrated in SIP-Raman studies, which usually analyzed cells grown with various ratios of ^{13}C/^{12}C- or ^{15}N/^{14}N-labeled substrates (e.g., glucose, naphthalene, bicarbonate, and ammonium). The cellular isotopic content was shown to correspond to either spectral peak ratios of Raman biomarkers (e.g., ^{13}C/^{12}C-labeled phenylalanine peak intensities) in heterotrophic cells (23, 26, 28, 31) or progressive shifts in the wavenumber position of carotenoids in photoautotrophic cells (11). Building on the above-mentioned studies, Taylor et al. (25) used resonance Raman microspectroscopy of carotenoid pigments to derive single-cell growth rates of photoautotrophic organisms from quantifying time-dependent ^{13}C assimilation. To date, there have been no SIP-Raman studies of heterotrophic bacterial growth dynamics relying on the quantitative tracing of ^{13}C assimilation into cellular biomass. To address this knowledge gap, we performed time course SIP experiments with *Escherichia coli* grown on complex organic substrates with a range of ^{13}C fractional abundances. Next, the progressive change in the isotopic fractional abundances of cells was measured by Raman microspectroscopy to derive single-cell bacterial growth rates.

RESULTS

Diagnostic Raman peak selection. Raman spectra of *E. coli* cells were acquired between 550 and 2,000 cm^{-1}, a region that contains peaks from many biomolecules such as nucleic acids, proteins, and lipids. Observed Raman peak positions were assigned to biomolecules and chemical moieties based on those reported in the literature (32–35) (Fig. 1 and Table 1).

TABLE 1 Wavenumber assignment to ^{12}C parent and red-shifted spectral peaks of macromolecules and chemical moieties reported in the literature[a]

Peak no.	Raman shift (cm^{-1})	Assignment(s)	Explanation
1	620 641	Phe τ(C-C) Tyr τ(C-C)	During labeling, the Tyr peak moves to the Phe position; a Phe red shift is not evident due to the weak signal
2	723 712 red shift	A ring breathing mode (DNA)	Adenine breathing mode; may also include C-S stretching from protein and other vibrations that broaden features, disqualifying it from quantitative analysis
3	779 761 red shift	C, T ring-breathing mode, ν(O-P-O) DNA backbone	Pyrimidine ring breathing; also, O-P-O symmetrical and asymmetrical stretching
4	1,002 966 red shift	Phe ring breathing mode (proteins)	Phenylalanine ring breathing—single sharp peak, making it amenable to quantitative analysis
5	1,090	ν(P-O^{2-}) (DNA), ν(C-O), (saccharides), ν(C-C) (saccharides, lipids)	Red shifts not evident, perhaps due to small relative amounts of lipids and carbohydrates
6	1,225 1,206 red shift 1,177 red shift	C, A, G (DNA); amide III (proteins); ν(P-O^{2-}) (DNA)	Too many overlapping vibrations for quantitative analysis
7	1,322 1,307 red shift	τ(CH$_2$) (proteins and nucleic acids), δ(C-H) (unsaturated fatty acids)	Too many overlapping vibrations for quantitative analysis; ring mode of DNA bases at 1,361 cm^{-1} shifted toward protein and fatty acid bands
	1,361	C, T, G (DNA)	
8	1,450 1,478	α(CH$_2$/CH$_3$), β(CH$_2$/CH$_3$) (proteins and lipids) A, G (N7 ring mode) (DNA)	Red shift not evident at 1,450 cm^{-1}; peak at 1,478 cm^{-1} red shifted toward 1,450 cm^{-1} but difficult to resolve
9	1,581 1,526 red shift	G, A ν(ring breathing mode) (DNA)	Vibration from purine bases shows significant and predictable red shifts
10	1,668 1,630 red shift	Amide I (proteins), T ν(C=O) (DNA); C ν(C=O) (DNA); Glu, Asp ν(C=O)OH (proteins)	Red shifts are evident but poor candidate for quantitation due to peak broadness and overlap of neighboring vibrations

[a] See references 32–35. Modes of vibration: α, scissoring; β, bending; δ, deformation; τ, twisting; ν, stretching. Abbreviations: Phe, phenylalanine; Tyr, tyrosine; A, adenine; G, guanine; T, thymine; C, cytosine.

Spectral features of *E. coli* cells cultivated at natural isotopic abundances did not change significantly through the growth phases (not shown), except for peaks emanating from nucleic acids. *E. coli* cells displayed distinct peaks assigned to vibrational modes of purine and pyrimidine bases (e.g., ring breathing modes of adenine at 723 cm^{-1} and cytosine and thymine at 779 cm^{-1}) in the exponential and stationary growth phases. Either these peaks were absent or their intensity was significantly reduced in lag-phase cells (0 to 30 min) (compare the spectral profiles in panels a and b in Fig. 1A and B at peaks 2, 3, and 6; detailed assignments can be found in Table 1).

Red shifts were detected in a multitude of Raman peaks that are inherent to nucleobases, amino acids, amides, and lipids. However, precise quantification of the relative contribution of ^{12}C- and ^{13}C-isotopologues was often hampered by several factors. For instance, red-shifted peaks of nucleobases (adenine, guanine, cytosine, and thymine), amino acids (tyrosine, glutamate, and aspartate), and amides (I and III) were evident, but precise quantification of their respective ^{12}C parent peaks was prevented by overlapping vibrational modes emanating from other moieties (e.g., peaks 1, 2, 3, 6, 7, and 10 in Table 1). Conversely, red shifts to wavenumbers already occupied by other functionalities impede the quantitation of some heavy isotopologues. This was observed for the tyrosine peak that shifted to a Phe position during labeling (peak 1 in Table 1).

Peaks of several nucleobase ring breathing modes moved to peak positions indicative of proteins, lipids, or unsaturated fatty acids (peaks 7 and 8 in Table 1). Furthermore, the CH_2 and CH_3 vibrational modes of proteins and lipids experience small, poorly resolved red shifts due to the relative differences in the atomic masses of C and H (peak 8 in Table 1). Low signal intensities of lipid and carbohydrate vibrational modes caused by C-C and C-O stretching did not permit reliable quantification of their respective isotopologues (peak 5 in Table 1).

Unlike the above-mentioned results, the ring breathing modes of Phe isotopologues with 6 ^{12}C atoms or 6 ^{13}C atoms in the phenyl ring display two well-defined peaks at 1,002 and 966 cm^{-1}, respectively. Their positions and intensities enable the reliable calculation of [^{13}C]Phe peak intensity fractions to use as a proxy for the cellular isotopic fractional abundance (f_{cell}). In order to achieve the utmost precision in quantifying peak intensities at 966 cm^{-1} and 1,002 cm^{-1}, we developed a robust curve-fitting procedure that allowed the precise deconvolution of partially overlapping peaks. Otherwise, a "contaminating" neighboring peak (1,006/1,009 cm^{-1}) would have prevented proper intensity measurements of the unlabeled Phe ring breathing mode at 1,002 cm^{-1} (see Fig. S2 in the supplemental material).

Validation of [^{13}C]Phe as a proxy for cellular ^{13}C fractional abundance. Among the diagnostic Raman peaks detected in this study, the essential amino acid phenylalanine (Phe), present in all cells, is the most promising reporter molecule for Raman-derived f_{cell} estimates. In order to validate [^{13}C]Phe as an accurate proxy for the cellular ^{13}C fractional abundance, we compared direct Raman-based measurements with two alternative determinations of f_{cell}. First, separate *E. coli* Bs-1 cultures were grown to early and late stationary phases in media with 11 different admixtures of the same ^{13}C and ^{12}C carbon substrates. Contributions of ^{13}C and ^{12}C additions to total carbon (f_{media}) in each medium were calibrated by total organic carbon analysis. Cells thus grown are well suited for testing the validity of Raman signature-derived f_{cell} estimates under various isotopic enrichments because they should have been very close to isotopic equilibrium with their medium ($f_{media} \cong f_{cell}$), and intrapopulation variability should be minimal compared to earlier growth stages. Raman-derived f_{cell} estimates after 4.5 and 18 h of incubation are statistically indistinguishable over the entire range of labeled media (f_{media} = 0.011 to 0.985), illustrating that the shorter incubation time was sufficient for *E. coli* Bs-1 populations to reach maximum labeling in their respective media (Fig. 2). Hence, a maximum duration of 4.5 h was chosen for all subsequent labeling experiments. Raman-based f_{cell} measurements were highly correlated with f_{media}, yielding regression slopes of 0.91 to 0.93 and very high coefficients of determination (R^2 = 0.99) (Fig. 2). The fact that the slope of f_{cell} over f_{media} is <1 suggests that either f_{cell} was slightly underestimated by our Raman approach; f_{media}, which was not measured directly in this experiment, was slightly overestimated; or cells did not reach isotopic equilibrium due to isotopic discrimination.

To assess whether the disparity between Raman f_{cell} and f_{media} resulted from inaccuracies in either ^{13}C-medium preparations (e.g., pipetting errors) or Raman measurements of f_{cell}, fractional isotopic abundances were independently measured by isotope ratio mass spectrometry (IRMS). Our carbon analyzer-corrected determinations of f_{media} were almost identical to those of the two ^{13}C-enriched admixtures (IRMS versus carbon analyzer, 0.217 ± 0.0001 versus 0.216, and 0.436 ± 0.003 versus 0.444). Both Raman- and IRMS-determined f_{cell} values varied linearly with IRMS-determined f_{media} (R^2 = 0.99) and, similar to the slopes in Fig. 2, were less than 1, at 0.897 and 0.896, respectively (Fig. 3a). Reassuringly, the accuracy of Raman f_{cell} determinations is strongly supported by direct comparison with IRMS-determined f_{cell} values, which are essentially identical within analytical uncertainty (Fig. 3b). We interpret the departure from the 1:1 line in Fig. 3a as emanating entirely from isotopic discrimination (α, fractionation). Alternatively, we are left with the unlikely possibility that both Raman and IRMS underestimate f_{cell} by exactly the same amount.

Derivation of bacterial growth parameters from SIP-Raman experiments. In order to monitor ^{13}C labeling of *E. coli* populations throughout all growth phases, cells

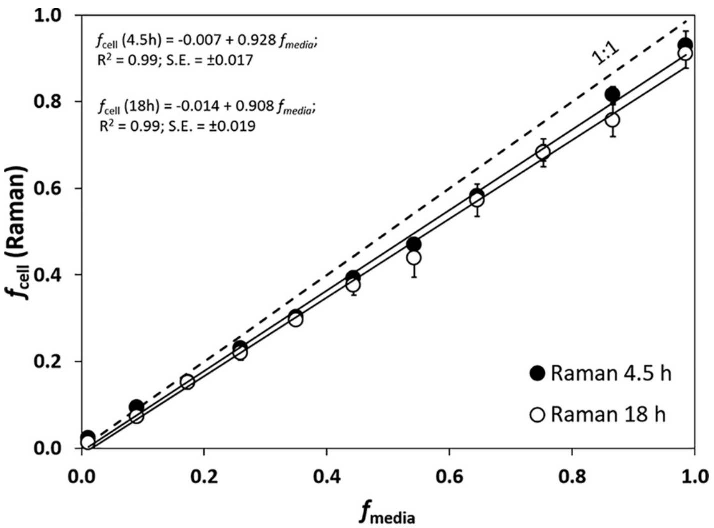

FIG 2 Relationship between cellular fractional ^{13}C labeling (f_{cell}) and growth media with various ^{13}C enrichments (f_{media}) determined in stationary-phase *E. coli* Bs-1 cells. Mean f_{cell} values (±1 SD) for cells grown for 4.5 h and 18 h were determined from Phe isotopologue peaks of ~800 Raman spectra acquired for each f_{media} treatment. The dashed line represents a 1:1 relationship between f_{media} and f_{cell}. Linear regression results are given in the plot. The difference between the f_{cell} slopes at 4.5 and 18 h was insignificant (*P* value of 0.44 by a significance test [68]).

were incubated with equivalent carbon concentrations of Bioexpress with various ^{13}C:^{12}C admixtures (f_{media} = 0.011, 0.348, and 0.985 for *E. coli* Bs-1, and f_{media} = 0.011 and 0.985 for *E. coli* K). Optical density (OD) measurements of cell suspensions of both *E. coli* strains confirmed that the growth curves were nearly identical among populations grown in the different medium admixtures (Fig. S3) (36). Thus, population growth among treatments can be considered replicated measurements of the same variable. Furthermore, previous studies with *E. coli* revealed that monitoring growth by the OD at different wavelengths can yield significantly different calculated growth rates (37). Thus, OD measurements were performed at 400 and 600 nm, wavelengths commonly used to measure bacterial cell density (38). In either case, both *E. coli* strains produced very similar, typical sigmoidal population growth curves.

Theoretical ^{13}C labeling kinetics were calculated using OD at 400 nm (OD_{400})- and OD_{600}-based growth curves to compute the number of generations (*n*) during each sampling interval using equation 6 and then compared to Raman-derived f_{cell} estimates. As expected, isotopic signatures of cells incubated in natural ^{13}C abundance media did not change over the time course (data not shown). Raman f_{cell} measurements agree remarkably well with predicted f_{cell} estimates in their general sigmoidal trajectory through time among all ^{13}C-enriched treatments as exemplified by *E. coli* Bs-1 (Fig. 4a and b). Within individual labeling treatments, Raman-based f_{cell} values strongly covaried (R^2 = 0.96 to 0.98) with those predicted from independent OD data, yielding regression slopes that are nearly 1, at 1.11 and 0.99, for treatments at f_{media} values of 0.348 and 0.985, respectively (Fig. 4a and b). The results from all time course treatments for *E. coli* Bs-1 and K were tested for their overall agreement between f_{cell} values derived from Raman measurements and those predicted from OD-based growth curves by means of a Bland-Altman difference plot (39) (Fig. 5). The mean differences in Raman-based f_{cell} from OD-predicted f_{cell} were −0.04 and −0.023 for the OD_{600} and OD_{400}, respectively (Fig. 5A and B). The mean difference of OD_{600}-derived f_{cell} determinations from those of OD_{400} was +0.017 (Fig. 5C). This comparison illustrates that while the OD_{600} and OD_{400} coherently track growth trends, subtle differences are evident among time intervals. In all cases, no more than two observations of the difference values (Raman-measured and predicted f_{cell} values) lie outside the 95% confidence limits.

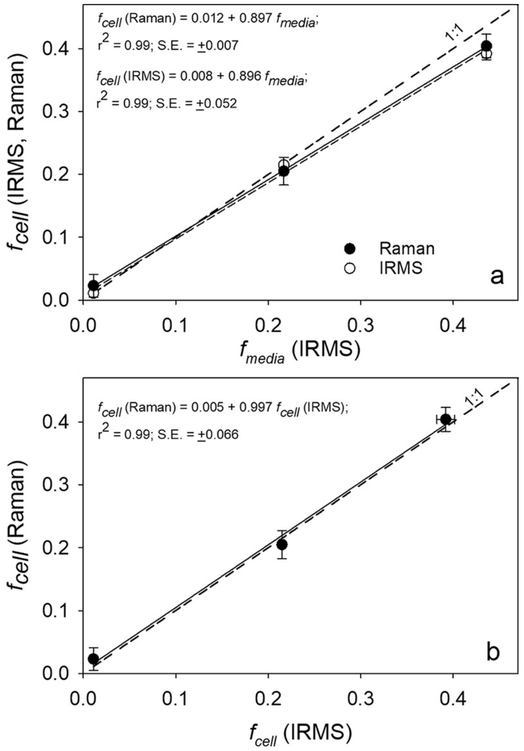

FIG 3 Comparisons of isotopic enrichments measured by Raman microspectroscopy and isotope ratio mass spectrometry (IRMS) for *E. coli* Bs-1 grown for 4.5 h. (a) Mean f_{cell} (±1 SD) determined by Raman microspectroscopy and IRMS as a function of f_{media}. ^{13}C enrichment was determined by IRMS in samples of dried media and *E. coli* cells and was measured in triplicate. Raman-derived f_{cell} values were based on spectra from 500 ± 45 cells in three different mapping regions per treatment. (b) Direct comparison of Raman microspectroscopic and IRMS determinations of f_{cell} using same data as those in panel a. The difference between the two slopes of f_{cell} (Raman and IRMS) in panel a was insignificant (*P* value of 0.99 by a significance test [68]).

The distribution patterns indicate that the agreement of both methods is consistent across the entire range of measurements and not biased toward higher or lower f_{cell} values (Fig. 5A and B).

Finally, growth rates derived independently from Raman and OD spectroscopic techniques were compared during exponential phase for both *E. coli* strains grown in the three ^{13}C-enriched media. Exponential phase was defined from natural-log-normal plots of the OD data. SIP-Raman-based single-cell growth rates were computed using equation 5 and equation 7. OD-based population growth rates were calculated with equation 2. Growth rates (μ) of both *E. coli* strains derived from the SIP-Raman measurements agreed remarkably well with those computed from both OD_{600} and OD_{400} measurements and were not significantly different from each other ($P > 0.05$ by one-way analysis of variance [ANOVA]) (Fig. 6a and b).

DISCUSSION

Challenges for accurate quantification of ^{12}C and ^{13}C Raman peaks. The consistent positions of Raman spectral peaks in *E. coli* cells grown at natural ^{13}C abundances illustrate this technique's analytical reproducibility. Thus, peak shifts to lower wavenumbers (red shifts) observed in cells grown in ^{13}C-enriched media can be attributed almost exclusively to the assimilation of heavy isotopes. However, among the various red-shifted biomolecules and chemical moieties, precise quantification of spectral peaks from isotopologues is often complicated by overlapping peaks of other origins (Fig. 1 and Table 1). Such occurrences have impeded peak quantification in prokaryotic and eukaryotic cells and limited Raman spectral features suitable for estimates of cellular ^{13}C

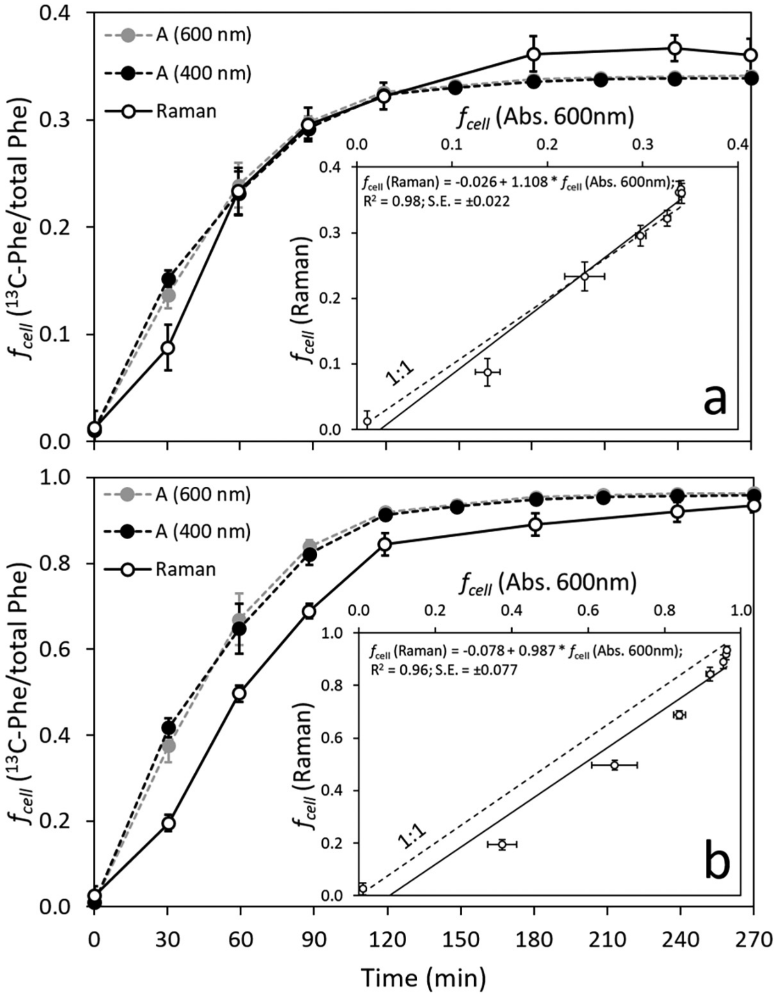

FIG 4 Population growth-dependent changes in cellular ^{13}C fractional abundances (f_{cell}) measured by Raman microspectroscopy and predicted from OD-based growth curves (absorbances at 600 and 400 nm) and equations 2 to 5. Results are for *E. coli* Bs-1 cells grown in labeled medium with f_{media} values of 0.348 (a) and 0.985 (b). Insets show linear regression results of comparisons between Raman-measured and predicted (OD_{600}) f_{cell} values. Linear regression results of the comparison between Raman-measured and predicted (OD_{400}) f_{cell} values (not shown in the graph) for *E. coli* Bs-1 cells grown at f_{media} values of 0.348 (a) and 0.985 (b) were as follows: f_{cell} (Raman) = $-0.03 + 1.12 \cdot f_{\mathrm{cell}}$ (OD_{400}), $R^2 = 0.97$, and standard error (SE) = ±0.027, and f_{cell} (Raman) = $-0.089 + 1.006 \cdot f_{\mathrm{cell}}$ (OD_{400}), $R^2 = 0.95$, and SE = ±0.084, respectively.

enrichment (20, 40, 41). Similar to Xie et al. (42), we found that some peaks emanating from DNA have very low intensities in the lag and early exponential phases of population growth, which impede proper quantification of DNA isotopologues (Fig. 1A). Raman spectral profiles are known to vary among cells in different growth stages or between cells assimilating different substrates (23, 42, 43). In our time course experiments, the effect of different substrates was largely avoided by inoculating preconditioned cells grown on the same medium (Bioexpress medium). The use of preconditioned inocula that were more or less synchronized to be in exponential phase likely also reduced the observed variations in Raman spectra at the earliest time points.

We chose Raman peaks that emanate from Phe isotopologues as a proxy for cellular isotopic abundance. Phenylalanine is an essential amino acid present in all organisms, making it a universal biomarker for all cells (41). As reported in numerous SIP-Raman studies focused on detecting cellular ^{13}C incorporation of prokaryotes and eukaryotes (20, 21, 23, 24, 26, 28, 40, 44–47), Phe produces distinct and easily quantifiable peaks in

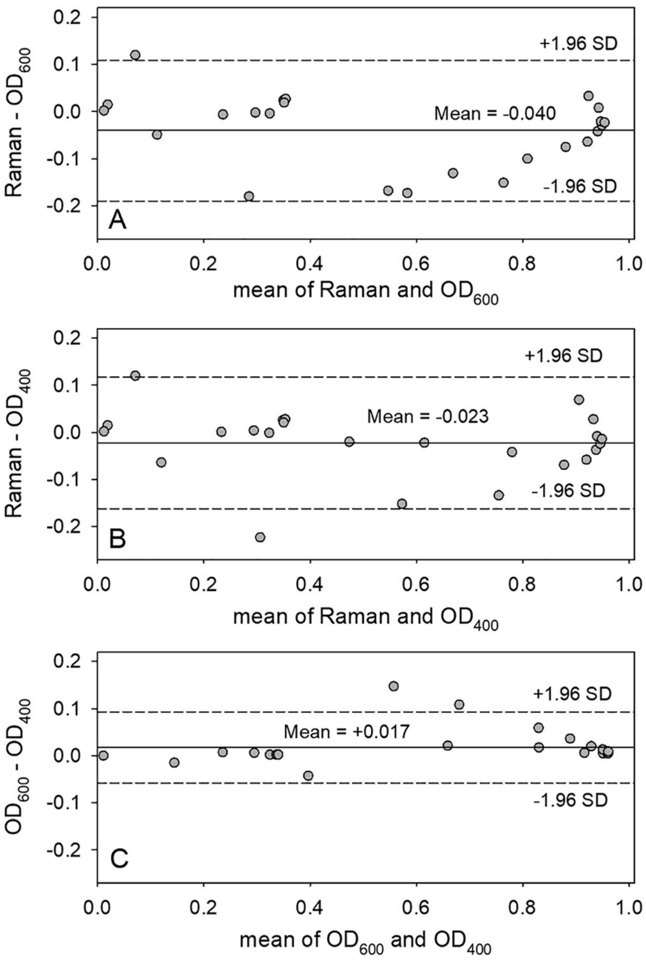

FIG 5 Bland-Altman difference plots comparing OD_{600}-, OD_{400}-, and Raman-derived f_{cell} estimates. Results of the three time course labeling experiments with *E. coli* K at an f_{media} value of 0.985 (n = 8), *E. coli* Bs-1 at an f_{media} value of 0.348 (n = 8), and *E. coli* Bs-1 at an f_{media} value of 0.985 (n = 8) are combined (n = 24). (A and B) Comparisons of predicted f_{cell} values from OD_{600} (A) and OD_{400} (B) measurements and Raman f_{cell} values. (C) Comparison of the two f_{cell} values predicted from the OD_{600} and OD_{400}. The solid horizontal line marks the mean difference between f_{cell} values derived by the two methods. Dashed horizontal lines represent the 95% confidence intervals (±1.96 standard deviations). One-way ANOVA found no statistical difference between f_{cell} values derived from Raman, OD_{600}, and OD_{400} results (P = 0.849).

Raman spectral profiles of *E. coli* cells of this study (Fig. 1C). The intensities of the phenyl ring breathing mode at 966 and 1,002 cm^{-1} representing 100% ^{13}C and 100% ^{12}C in the ring, respectively, were used to compute the ^{13}C fractional abundance of Phe. This ratio was then extrapolated to the ^{13}C isotopic abundance of cells (f_{cell}) based on the assumption that all cellular carbon pools are equally isotopically enriched. However, two more Raman peaks (989 and 978 cm^{-1}) can occur that are attributed to partially labeled Phe isotopologues in cells fed with [^{13}C]glucose (40, 48). In our study, these peaks could not be confidently detected above baseline and analytical noise. The rich Bioexpress labeling medium used here consists of hydrolyzed ^{13}C-labeled cyanobacterial biomass and thus represents a complex amalgam of organic substrates, presumably including peptides and free amino acids. The assimilation of ^{13}C-labeled amino acid mixtures (49) or ^{13}C-labeled phenylalanine (50) results in the appearance of the red-shifted Phe peak at 967 cm^{-1} as well as the ancestral peak at 1,002/1,003 cm^{-1} but no intermediate peaks indicating 2 or 4 ^{13}C substitutions in the phenyl ring. Thus, we interpret our spectral data as indicating that cells are not synthesizing Phe *de novo*

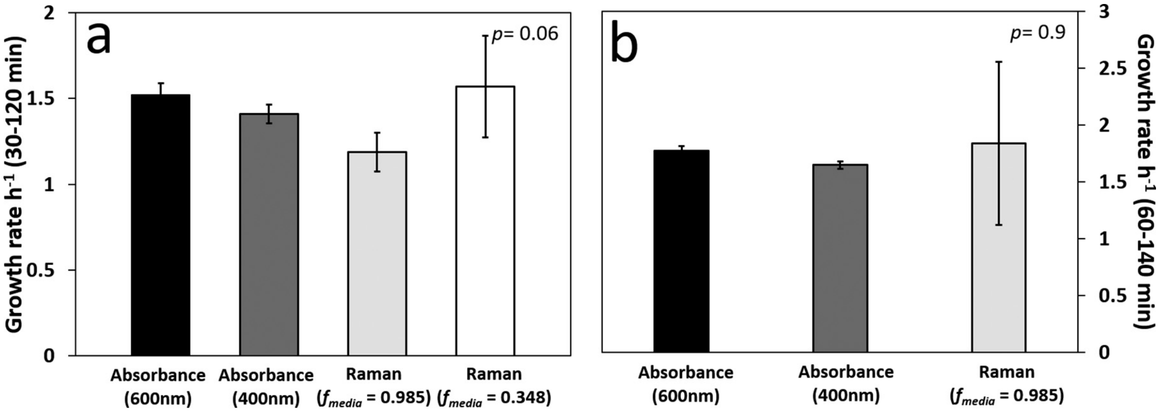

FIG 6 Comparison of mean growth rates (±1 SD) derived from OD_{600}, OD_{400}, and Raman results for *E. coli* Bs-1 (a) and *E. coli* K (b) during exponential phase. OD-derived growth rates are based on the population growth of three and two parallel incubations of *E. coli* Bs-1 (a) and *E. coli* K (b), respectively. Raman-derived growth rates are based on approximately 2,400 interrogated cells per time point in each labeling treatment (f_{media} = 0.348 and 0.985 for *E. coli* Bs-1, and f_{media} = 0.985 for *E. coli* K). *P* values from a single-factor ANOVA are given in the top right corner of each plot.

when presented with preformed [^{12}C]Phe and [^{13}C]Phe in the medium. Under our experimental conditions, cells appear to be opting for energy-saving salvage pathways to meet their Phe requirement.

Phenylalanine as a quantitative reporter for cellular isotopic abundance. The use of Phe as a proxy for f_{cell} was validated by two independent methods. Analogous to the approach of Huang et al. (28), we calibrated *E. coli* f_{cell} estimates against isotopic signatures of the media using a broad range of isotopic enrichments spanning natural abundance to 98.5% ^{13}C (Fig. 2). This approach assumes that cells reach isotopic equilibrium with their medium ($f_{cell} = f_{media}$) after populations are well into stationary phase (in our case, 4.5 and 18 h). We also compared Raman-based values to direct f_{cell} determinations by IRMS of cells with three different isotopic contents (f_{media} = 0.011, 0.216, and 0.444) (Fig. 3). In both cases, Raman-based f_{cell} values were highly reproducible and covaried predictably with f_{media}. In the pseudocalibration curve, Raman f_{cell} values were on average 11% isotopically lighter than the media in which they grew. Comparing IRMS data for f_{media}, Raman and IRMS f_{cell} values were both on average 6% lighter than those of their growth media. Are these disparities indicative of isotopic disequilibrium due to insufficient time or fractionation? In Bioexpress medium, both *E. coli* strains entered stationary phase within 3 h of inoculation, so when these cells were harvested (4.5 and 18 h), they should have been as isotopically equilibrated as possible. However, the observed 6 to 11% depletions result in isotopic fractionation factors (α) of 0.89 to 0.94, which, to our knowledge, represent significantly more fractionation than previously reported. Independent IRMS measurements of f_{cell} confirmed the accuracy of Raman-derived estimates of ^{13}C enrichments, being statistically indistinguishable within analytical uncertainty. IRMS is known to provide highly sensitive and precise measurements of isotopic ratios and is thus considered the gold standard for validating the analytical accuracy of Raman-based f_{cell} determinations. To the best of our knowledge, direct comparison of cellular isotopic enrichments by Raman and IRMS has been previously performed only with extracted proteins (11) but never using total cellular biomass. The close agreement between IRMS- and Raman-based determinations of f_{cell} strongly supports our assumption that all cellular carbon pools acquire comparable ^{13}C signatures indicated by the reporter molecule Phe.

Explaining why stationary-phase cells were isotopically depleted relative to their media, whether measured by Raman or IRMS, is challenging. We can safely rule out that carryover of unlabeled biomass from the inoculum accounted for the depressed f_{cell} values since a negligible amount (dilution of 1:100) of a culture grown overnight was used to start the incubations. To illustrate, after exponential growth for 7 generations (3.4 h for our cultures), legacy ^{12}C biomass can account for only 0.75% of the resulting biomass, totally independent of the inoculum size. This is clearly insufficient to explain the 6 to 11% depletion in the ^{13}C biomass signature.

Alternatively, isotopic depletion of biomass might be explained by the anaplerotic assimilation of ambient inorganic ^{12}C during growth. This heterotrophic CO_2 fixation process can account for 1 to 8% of the total carbon assimilated by microorganisms (51). During anaplerotic reactions, CO_2 is consumed in the tricarboxylic acid (TCA) cycle when phosphoenolpyruvate (PEP) or pyruvate is carboxylated by PEP carboxylase or pyruvate carboxylase. However, under our incubation conditions (aeration, rich complex medium, and glycolytic conditions), Phe biosynthesis is decoupled from TCA cycle metabolites, deriving its precursor from the shikimate pathway, which is fed by PEP from glycolysis and erythrose 4-phosphate from the pentose phosphate pathway (52, 53). We conclude that if anaplerosis were operative in lowering the ^{13}C fractional abundance in most cellular components except phenylalanine, this would be reflected by the higher fractional abundance of [^{13}C]phenylalanine (as a proxy for f_{cell}) in our Raman analysis compared to f_{cell} values determined by IRMS. To the contrary, Raman and IRMS delivered almost identical values of f_{cell}. Furthermore, if the *de novo* synthesis of Phe received any carbon from anaplerotic reactions, intermediate isotopologues would be evident from Raman peaks at 989 and 978 cm^{-1}, but they were not. Thus, we judge anaplerosis to have played a negligible to nonexistent role in our observations.

Carbon isotopic fractionation in heterotrophic bacterial metabolism is a possible mechanism to produce light cellular biomass. The kinetic isotope effect influences specific enzymatic reaction rates, resulting in isotopic compositions of certain biomolecules, such as proteins, lipids, or amino acids, distinctive from the substrate utilized (54–57). Although isotopic fractionation can vary considerably among individual cellular pools, Blair et al. (54) reported that *E. coli* proteins were only 0.11% lighter than their glucose growth substrate, effectively too small to explain the observed f_{media}-f_{cell} disparities. It is noteworthy that almost all previous studies examining cellular isotopic fractionation did so at natural isotopic abundances and did not focus on bacterial metabolic fractionation of ^{13}C-enriched tracers. While not evaluating fractionation *per se*, a study using SIP to monitor phospholipid fatty acid synthesis found that [^{13}C]toluene additions preferentially exerted inhibitory effects on fatty acid biosynthesis and bacterial growth relative to [^{12}C]toluene additions (58). In contrast, our OD-based measurements yielded statistically indistinguishable population growth curves among parallel incubations with different isotope admixtures (see Fig. S3 in the supplemental material). We also found remarkable agreement between f_{cell} values determined by Raman and IRMS (Fig. 3) and between predicted and Raman-measured f_{cell} values during the time course experiment (Fig. 4 and 5). Furthermore, Raman-based growth rate estimates derived from f_{cell} were statistically indistinguishable from those computed from OD measurements (Fig. 6). Nevertheless, future studies should carefully address potential biases arising from isotope fractionation and anaplerosis with different bacterial groups, carbon substrates, and metabolic pathways.

Quantitative SIP-Raman applications in microbial ecology. We demonstrate that single-cell bacterial growth rates can be derived from known fractional isotopic abundances of the growth substrate (f_{media}) and the cells (f_{cell}) measured at just two time points using Raman microspectroscopy. In a fashion similar to that of a recent SIP-NanoSIMS study (14), SIP-Raman approaches can also measure single-cell carbon assimilation rates, when combined with precise total carbon estimates of the organism under scrutiny (F. Weber, T. Zaliznyak, and G. T. Taylor, unpublished data).

The current study used a complex medium (^{13}C-labeled Bioexpress medium), but specific ^{13}C-substrates can certainly be employed to study the bacterial growth response and physiological heterogeneity within and among populations. For example, in studies focusing on substrate preference, diauxic growth, and carbon catabolite repression, quantitative SIP-Raman microspectroscopy used with selected labeled and unlabeled carbon substrates would permit the determination of the extent to which mixed substrates are utilized on the single-cell level (27). Another elegant strategy for measuring bacterial growth in laboratory or field experiments might be provided by Raman microspectroscopic monitoring of [^{13}C]Phe fractional abundances in cells after the addition of ^{13}C-labeled Phe in amounts exceeding natural concentrations. While the assimilation of [^{13}C]Phe into bacterial protein pools has been demonstrated by Raman microspectroscopy (49, 50), the practicality for studying growth dynamics has not yet been tested. If we assume that [^{13}C]Phe additions alone do not promote growth, as assumed by the [^{3}H]leucine and [^{3}H]thymidine growth methods (59, 60), then estimates of growth supported solely by autochthonous organic material can be derived. Clearly, empirical testing of whether [^{13}C]Phe additions stimulate growth in such SIP experiments is required before proceeding.

In principle, our approach can be applied to microbiome and field experiments examining bacterial growth and population dynamics based on the uptake of either complex or individual labeled carbon substrates. The complex labeling medium used here (Bioexpress) is a hydrolysate of ^{13}C-labeled cyanobacterial biomass. Thus, to some extent, it mimics the complex amalgam of dissolved organic matter released by phytoplankton in natural waters. Alternatively, the use of specific ^{13}C-compounds enables the study of growth responses of key players utilizing different carbon sources by determining substrate-specific growth rates. However, depending on the research question, substrate-dependent enrichments of specialized populations within the microbial community may be desired or tolerable but are sometimes problematic. SIP studies generally depend on tracer amendments at levels exceeding the natural substrate abundances and incubation times sufficient for microbial utilization of the labeled substrate. This potentially perturbs the natural community by selectively stimulating the activity of populations favored by the newly imposed conditions. The choice of appropriate tracer additions represents a trade-off between detectability and perturbations to natural microbial assemblages. Therefore, the choice reflects a balance between the detection method's sensitivity, the trophic status of the sample, and the quantity of cellular biomass that finally utilizes the tracer (10). Current SIP methods that can be combined with phylogenetic identification, either by SIP-DNA/RNA or by fluorescence *in situ* hybridization (FISH) coupled to Raman or NanoSIMS, vary widely in their detection limits of isotopic tracers. Whereas NanoSIMS is the most sensitive among these, detecting as little as 0.1 atom% (61), SIP-RNA and SIP-DNA require up to 20 atom% (50 atom% for high-GC-content DNA) for the efficient separation of heavy and light fractions (62–64). For spontaneous Raman microspectroscopy, a minimum cellular isotopic content of 10 atom% has been suggested as the threshold for discriminating between labeled and unlabeled bacterial cultures (28). Consequently, for monitoring of cellular labeling propagation to derive microbial rate measurements in environmental samples, significantly higher isotopic content may be required. However, advanced signal enhancement techniques involving colloidal metal nanoparticles, i.e., surface-enhanced Raman spectroscopy (SERS), can increase the Raman signal intensity by many orders of magnitude (10^{7} to 10^{11}) and thus potentially can improve the limit of detection of cellular isotopic labeling (9, 41). This would be transformative because it would make the much less labor-intensive and nondestructive Raman approach the method of choice for monitoring label propagation in preserved, frozen, or live cells. SIP-SERS also has the potential to better resolve additional quantitative Raman biomarkers, as recently demonstrated for adenine, which exhibited strong red shifts in *E. coli* cells fed with [^{13}C]glucose (48, 65). Quantitative SIP-Raman approaches combined with methods for phylogenetic identification such as FISH or downstream sequencing of Raman-sorted cells (12) represent extremely promising tools for enriching our understanding of microbial rates relevant for matter cycling in the environment.

Conclusion and future perspectives. Our proof-of-concept study demonstrates that the SIP-Raman approach enables reliable bacterial growth rate measurements based on the assimilation of ^{13}C-labeled organic matter by the quantitation of the fractional abundance of Phe isotopologues over time. This approach is highly applicable to many questions in biomedical, applied, and environmental microbiology that aim to assess bacterial growth, substrate preference, and metabolic fluxes. Furthermore, it allows analysis at both the single-cell and population levels without prior isolation.

When the nature of the sample limits the application of traditional methods (e.g., cell counts, most probable number, optical density, and respiration rates), such as in complex matrices (e.g., soil, sediment, and biofilms) or mixed microbial assemblages, SIP-Raman is an especially elegant alternative.

Several studies have shown the compatibility of SIP-Raman with FISH or with molecular analysis of marker genes within libraries constructed from cells that were Raman sorted according to isotopic signatures (12, 13, 24, 28, 31). Combining these tools enables investigators to directly link genetic identity to functional traits of single cells in mixed microbial assemblages. However, these combined approaches have thus far been performed largely in a qualitative manner, i.e., cataloguing active and nonactive cells. Further refinement of quantitative SIP-Raman approaches has the potential to accurately measure microbial metabolic rates. Quantitative SIP-Raman approaches complemented by phylogenetic identification tools overcome a major technical constraint, linking phylogenetic identity with functions and metabolic rates of cells in environmental samples. SIP-Raman approaches offer tremendous potential to study trophodynamics in microbial interactions, such as the interspecies carbon transfer in predator-prey relationships (our unpublished data) and among symbiotic partners. We believe that this approach will pave the way toward a deeper understanding of numerous microbial processes.

MATERIALS AND METHODS

Bacterial growth in isotopically enriched media. Two *E. coli* strains, K and Bs-1, were chosen for isotopic labeling experiments. The UV-sensitive mutant strain *E. coli* Bs-1, acquired from the American Type Culture Collection (ATCC 23224), was selected for grazing experiments (F. Weber, T. Zaliznyak, V. P. Edgcomb, and G. T. Taylor, unpublished data) because UV radiation induces irreparable DNA lesions and results in the cessation of growth. Both strains were routinely grown in Bacto nutrient broth medium (Difco Laboratories USA). In isotopic labeling experiments, *E. coli* strains were grown in replicate flasks of a complex Bioexpress medium (chemical purity of $\gtrsim$98%; Cambridge Isotope Laboratories), which contained nearly equivalent total carbon concentrations but various proportions of labeled and unlabeled substrates. Bioexpress media are derived from hydrolysates of cyanobacterial cultures grown in either ^{12}C- or ^{13}C-bicarbonate, and their exact compositions are proprietary. The fractional isotopic abundances of the media [$f_{\text{media}} = {}^{13}\text{C}/({}^{12}\text{C} + {}^{13}\text{C})$] were established by mixing various proportions of ^{13}C-Bioexpress medium (98.5% ^{13}C enrichment in all carbon substrates) with ^{12}C-Bioexpress medium (98.9% ^{12}C). The total carbon concentrations of both labeled and unlabeled media were directly determined using a Thermo EA1112 carbon-nitrogen-sulfur (CNS) elemental analyzer (66). To accomplish this, quartered precombusted (450°C for 4 h) Whatman GF/F glass fiber filters were placed in 10- by 12-mm tin capsules (CE Elantech, Inc.), soaked with 100 μl of the respective Bioexpress media (10× working stock solution), and dried overnight at 65°C. Blanks were prepared in the same manner without the addition of medium. All measurements were performed in duplicate. Nominal volumetric (*vol*) f_{media} values of medium admixtures were corrected using measured total carbon concentrations ([C_{Tenr}] and [C_{T0}]) of both media, their respective ^{13}C fractional abundances (f_{enr} = 0.985 and natural f_0 = 0.011), and the following equation:

$$f_{\text{media}} = \frac{vol[C_{Tenr}]f_{enr} + vol[C_{T0}]f_0}{vol[C_{Tenr}] + vol[C_{T0}]} \tag{1}$$

If not stated otherwise (e.g., determined by IRMS), all f_{media} values of medium preparations presented in this study are corrected based on carbon analyzer values for total organic carbon.

Validation of Raman microspectroscopy for determining cellular ^{13}C fractional abundance. To test the accuracy of Raman-derived estimates of cellular fractional ^{13}C abundances [$f_{\text{cell}} = {}^{13}\text{C}/({}^{13}\text{C} + {}^{12}\text{C})$], *E. coli* Bs-1 cells were grown in media with a range of ^{13}C fractional abundances and sampled during early and late stationary phases as cells approached isotopic equilibrium with their medium. Specifically, 50 μl of an *E. coli* Bs-1 culture grown overnight in unlabeled Bioexpress medium was inoculated into 5 ml of 11 different ^{13}C-labeled Bioexpress medium admixtures ranging from natural ^{13}C abundance to 98.5% (f_{media} = 0.011, 0.09, 0.17, 0.26, 0.35, 0.44, 0.54, 0.65, 0.75, 0.87, and 0.985). Suspensions were incubated in 30-ml tissue culture flasks with vented caps at 37°C in the dark on an orbital shaker at 100 rpm. Subsamples (900 μl) from each bacterial suspension were fixed with borate-buffered, filtered formaldehyde (2% final concentration) after incubation for 4.5 and 18 h. Fixed cells were collected on 0.2-μm polycarbonate filters (25 mm, Millipore Isopore) and stored at -20°C for Raman interrogations.

As an independent validation of Raman-derived f_{cell} estimates, ^{13}C fractional abundances of *E. coli* Bs-1 cells and their media were directly determined by isotope ratio mass spectrometry (IRMS). For measurements of the isotopic ratios of the media, quartered precombusted GF/F filters were placed in 10- by 12-mm tin capsules (CE Elantech, Inc.), soaked with 80 μl of three ^{13}C/^{12}C-Bioexpress growth medium admixtures (f_{media} = 0.011, 0.216, and 0.444), and dried overnight at 65°C. For blanks, precombusted GF/F filter sections were treated the same way but omitting the medium. Wrapped tinfoil cups were stored at room temperature until IRMS analysis.

For IRMS measurements of f_{cell}, 15 ml of the same medium preparations was seeded with 150 μl of an *E. coli* Bs-1 culture grown overnight (grown in unlabeled Bioexpress medium) and incubated for 4.5 h, as described above. After incubation, *E. coli* Bs-1 cells were immediately inactivated by UV irradiation to avoid further growth during subsequent handling and to obviate the need for a fixative, such as formaldehyde, that would dilute the ^{13}C signature. Cell suspensions in tissue culture flasks were exposed to UV radiation for 60 s under constant shaking to a total intensity of 21,000 ergs mm^{-2} on a UVP M-26XV benchtop UV transilluminator. Cells from 12 ml of each culture were captured on precombusted GF/F filters and rinsed with filter-sterilized (0.2-μm) distilled water to remove excess medium. For blanks, GF/F filters were rinsed with the same volume of filter-sterilized distilled water. Filters were dried overnight at 65°C and cut into equal quarters before wrapping them in tinfoil cups for IRMS analysis. Replicate aliquots (900 μl) of each bacterial suspension were also fixed with formaldehyde (2% final concentration) and stored for Raman interrogations.

IRMS measurements of media, cell samples, and blanks were performed in triplicate by UC Davis Stable Isotope Facility (https://stableisotopefacility.ucdavis.edu/). Technical limitations of the IRMS system prevent reliable carbon isotopic quantifications exceeding 50 atom%, and therefore, media and bacterial preparations with higher labeling were not submitted for analysis.

^{13}C label assimilation dependence on growth rates. Inocula (250 μl) of cultures grown overnight in unlabeled Bioexpress medium were introduced into 25 ml of labeled medium admixtures (f_{media} = 0.011, 0.348, and 0.985 for *E. coli* Bs-1, and f_{media} = 0.011 and 0.985 for *E. coli* K). Cells were incubated in 60-ml vented tissue culture flasks at 37°C on an orbital shaker at 100 rpm for 4.5 h in the dark. Immediately after inoculation and every 20 to 30 min thereafter, the *E. coli* cell abundance was indirectly monitored by triplicate optical density (OD) measurements at 400 and 600 nm on a Perkin-Elmer Lambda 2 UV-visible (UV-Vis) spectrophotometer using Sub-Micro cuvettes. Time course OD measurements provided an independent means to calculate population doubling times (g) and first-order growth rates (μ). Replicate subsamples were also formaldehyde fixed at all time points and filtered onto 0.2-μm polycarbonate filters for Raman interrogations.

Raman interrogations of bacteria. Polycarbonate membranes typically used to concentrate microorganisms are Raman active and severely interfere with the analysis. Therefore, preserved cells from all experiments were freeze transferred from membrane filters to mirror-finished stainless steel slides (1 by 3 in.) as detailed previously (67) and stored at −20°C until performing Raman interrogations. This technique semiquantitatively transfers cells onto a "Raman-silent" surface and enables the acquisition of high-quality single-cell Raman spectra free from background interference.

Raman measurements were performed at the NAno-Raman Molecular Imaging Laboratory (NARMIL) at Stony Brook University. Analyses were performed using a Renishaw inVia confocal Raman microspectrophotometer configured with a modified upright Leica DM2700 epifluorescence microscope, a computer-controlled motorized *xyz* stage (0.1-μm minimum step size), a 633-nm He/Ne laser, and a 1,040-by-256 charge-coupled-device (CCD) Peltier-cooled detector. Single *E. coli* cells (30 to 40 individuals) from each sample were targeted from reflected bright-field inVia camera micrographs (magnification, ×1,000) and individually interrogated at 100% laser power (~4 mW at sample) through a Leica dry 100× (numerical aperture [NA] = 0.9) lens objective, which produced a laser spot diameter of 0.86 μm. Spectra were obtained using 1,200-line/mm diffraction grating, aligned to the wavenumber region between ~220 and 2,060 cm^{-1} (1,200 cm^{-1} center), yielding a spectral resolution of 1.2 cm^{-1}. CCD detector exposures were 2 s each, and 20 exposures were acquired for each spectrum. Additionally, cell clusters were identified as regions of interest (ROIs), and their location and size were determined from the micrographs (see Fig. S1 in the supplemental material). Raman spectra for ROIs were acquired automatically in StreamHR mapping mode at grid nodes (1-μm step size) using Renishaw WiRE Raman software (version 5.2). The optical configuration and spectral acquisition in the mapping mode followed the same specifications as the ones described above, except for the exposure time, which was set to 18 s per grid node. For each sample in the validation experiment and for each time point in the growth experiment (2 to 4 and usually 3), Raman maps were produced from approximately 1,000 to 5,000 individual spectra (average of ~3,000), generating spectra from approximately 300 to 800 (average of ~500) individual cells (Fig. S1). Processed data from both single-cell and mapped spectral data delivered comparable average results, but the latter had narrower confidence intervals (lower relative standard deviations [SD]) due to the larger sample size. Furthermore, Raman mapping reduces observer bias because all cells lying on grid nodes are automatically interrogated, thereby randomizing cell selection. Thus, all results presented in this study are based on Raman maps, except for the illustration of "red shifts" in Raman spectral profiles over time in Fig. 1, which are based on single-cell spectra from 30 to 40 individuals.

Raman spectral analysis. Each mapped sample contained spectra from approximately 500 cells. All spectra were saved as separate text files using Renishaw WiRE Raman software (version 5.2). Further data processing was performed using a custom Python script that performed the following tasks. From an individual map, all spectra not exceeding a filtering threshold of 40 counts above the baseline were excluded as these originate from barren nodes within the map's grid. The map's averaged spectrum was then truncated into two regions, the Phe-diagnostic region from 950 to 1,050 cm^{-1} and the signal-free region from 1,800 to 2,000 cm^{-1}, to calculate the analytical noise level. A linear baseline correction was applied to the "noise" region to determine the background signal variance (±1 SD). The mean spectrum within the diagnostic region was normalized to a value of 1 using the highest peak, and analytical noise among the ~500 spectra was scaled accordingly. A quadratic polynomial was applied for baseline correction of the diagnostic region. This spectral region was then subjected to a nonlinear least-squares peak-fitting routine that iteratively fit five Voigt probability distribution profiles positioned at 966, 990, 1,002, 1,007/1,009, and 1,029 cm^{-1} to the original curve. Positions and widths of the peaks at 966 and

1,002 cm^{-1} were allowed to vary simultaneously during fitting iterations, but the distance between 100% ^{13}C- and ^{12}C-isotopologue peaks (966 and 1,002 cm^{-1}) was fixed at 36.5 cm^{-1}, and sigma and gamma Voigt parameters were limited to 15. The peak at 1,029 cm^{-1} is a secondary mode of the Phe ring, and the unassigned peaks at 990 and 1,007/1,009 cm^{-1} were introduced to optimize the convergence of the total fit. The peak position typically occurring between 1,006 and 1,009 cm^{-1} was allowed to vary between 1,004 and 1,012 cm^{-1}, and positions of the peaks at 1,029 and 990 cm^{-1} were allowed to vary $\pm$10 cm^{-1}. Widths of unassigned and secondary peaks were allowed to vary between 0.1 and 15 cm^{-1}. The statistical goodness of fit was assessed on the fly by a reduced chi-square comparison of the total fit with original data. The fitting routine ceased when the reduced chi-square tolerance level (1.0e^{-7}) and minimum divergence were attained.

As the ^{13}C fractional abundance of Phe increases within cellular protein, the peak at 966 cm^{-1} intensifies as the intensity of the peak at 1,002 cm^{-1} weakens. At higher fractional abundances, the low-intensity 1,002 cm^{-1} of [^{12}C]Phe was observed to be masked by the neighboring peak at 1,006 cm^{-1}. However, our curve-fitting routine allowed us to deconvolve the two peaks and obtain the intensity of the [^{12}C]Phe ring breathing vibration at lower abundances. Fractional abundances of [^{13}C]Phe and standard deviations were calculated from the curve-fitted peak heights (intensity ratios as $I_{966}/I_{966} + I_{1,002}$) and used as a proxy for the total cellular ^{13}C isotopic content (f_{cell}).

Labeling kinetics and Raman-derived growth rates. Considering that bacterial growth parameters can vary through time course experiments (e.g., lag, exponential, and stationary phases), growth rate constants (μ_i) and generation times (g_i) were calculated between all consecutive time points (e.g., t_0, t_1, t_2, . . ., t_x) using the OD measurements (e.g., A_0, A_1, A_2, . . ., A_x) at 400 and 600 nm and the following two equations, respectively:

$$\mu_1 = \frac{(\ln A_1 - \ln A_0)}{(t_1 - t_0)} \tag{2}$$

$$g_1 = \frac{\ln(2)}{\mu_1} \tag{3}$$

The cumulative number of generations (n) completed during growth in the ^{13}C-labeled medium was calculated by summing n_i for each time interval (e.g., from t_0 to t_i) of consecutive time points and their respective generation times (g_i) using the following equation:

$$n = \sum_{t=1}^{t=x} \left[\frac{(t_1 - t_0)}{g_1} + \ldots + \frac{(t_x - t_{x-1})}{g_x} \right] \tag{4}$$

To calculate Raman-derived growth rates (μ [h^{-1}]) for each time interval within a growth curve, n must first be calculated from f_{cell}, f_0, f_{media}, and α values using equation 5, which was derived from equation 6 (25). The ^{13}C fractional abundance of the ancestral growth medium (f_0) is assumed to be constant at a natural abundance of 0.011, and medium ^{13}C enrichment (f_{media}) is either titrated from known admixtures of enriched and light media or measured directly. The isotopic fractionation factor (α) in proteins for heterotrophic bacteria is assumed to be 0.9989 (54).

$$n = -\frac{1}{\ln(2)} \ln \left[\frac{f_{\text{cell}} - \alpha f_{\text{media}}}{\alpha(f_0 - f_{\text{media}})} \right] \tag{5}$$

$$f_{\text{cell}} = \alpha f_{\text{media}} + \alpha(f_0 - f_{\text{media}}) e^{-n \ln(2)} \tag{6}$$

Next, to obtain μ from n at each time interval (t), the following equation was applied:

$$\mu = \frac{n \cdot \ln(2)}{t} = \frac{\ln(2)}{g} \tag{7}$$

SUPPLEMENTAL MATERIAL

Supplemental material is available online only.

SUPPLEMENTAL FILE 1, PDF file, 0.8 MB.

ACKNOWLEDGMENTS

We thank Caitlin Asato for CNS analysis at the Center for Clean Water Technology within the School of Marine and Atmospheric Sciences and the Department of Civil Engineering. IRMS analyses of media and bacteria were conducted by the UC Davis Stable Isotope Facility.

Raman data were acquired in SoMAS' NAno-Raman Molecular Imaging Laboratory (NARMIL), a community resource dedicated to environmental science applications and founded with NSF-MRI grant OCE-1336724. This research was primarily supported by Gordon and Betty Moore Foundation grant number 5064.

REFERENCES

1. Brock TD. 1971. Microbial growth rates in nature. Bacteriol Rev 35:39–58. https://doi.org/10.1128/br.35.1.39-58.1971.
2. Kemp PF, Cole JJ, Sherr BF, Sherr EB (ed). 1993. Handbook of methods in aquatic microbial ecology, 1st ed. CRC Press, Boca Raton, FL.
3. Kirchman DL. 2016. Growth rates of microbes in the oceans. Annu Rev Mar Sci 8:285–309. https://doi.org/10.1146/annurev-marine-122414-033938.
4. Campbell BJ, Kirchman DL. 2013. Bacterial diversity, community structure and potential growth rates along an estuarine salinity gradient. ISME J 7: 210–220. https://doi.org/10.1038/ismej.2012.93.
5. Long AM, Hou S, Ignacio-Espinoza JC, Fuhrman JA. 2021. Benchmarking microbial growth rate predictions from metagenomes. ISME J 15:183–195. https://doi.org/10.1038/s41396-020-00773-1.
6. Lee N, Nielsen PH, Andreasen KH, Juretschko S, Nielsen JL, Schleifer KH, Wagner M. 1999. Combination of fluorescent in situ hybridization and microautoradiography—a new tool for structure-function analyses in microbial ecology. Appl Environ Microbiol 65:1289–1297. https://doi.org/10.1128/AEM.65.3.1289-1297.1999.
7. Malmstrom RR, Cottrell MT, Elifantz H, Kirchman DL. 2005. Biomass production and assimilation of dissolved organic matter by SAR11 bacteria in the Northwest Atlantic Ocean. Appl Environ Microbiol 71:2979–2986. https://doi.org/10.1128/AEM.71.6.2979-2986.2005.
8. Sintes E, Herndl GJ. 2006. Quantifying substrate uptake by individual cells of marine bacterioplankton by catalyzed reporter deposition fluorescence in situ hybridization combined with microautoradiography. Appl Environ Microbiol 72:7022–7028. https://doi.org/10.1128/AEM.00763-06.
9. Taylor GT. 2019. Windows into microbial seascapes: advances in nanoscale imaging and application to marine sciences. Annu Rev Mar Sci 11: 465–490. https://doi.org/10.1146/annurev-marine-121916-063612.
10. Glibert PM, Middelburg JJ, McClelland JW, Vander Zanden MJ. 2019. Stable isotope tracers: enriching our perspectives and questions on sources, fates, rates, and pathways of major elements in aquatic systems. Limnol Oceanogr 64:950–981. https://doi.org/10.1002/lno.11087.
11. Li M, Canniffe DP, Jackson PJ, Davison PA, Fitzgerald S, Dickman MJ, Burgess JG, Hunter CN, Huang WE. 2012. Rapid resonance Raman microspectroscopy to probe carbon dioxide fixation by single cells in microbial communities. ISME J 6:875–885. https://doi.org/10.1038/ismej.2011.150.
12. Lee KS, Palatinszky M, Pereira FC, Nguyen J, Fernandez VI, Mueller AJ, Menolascina F, Daims H, Berry D, Wagner M, Stocker R. 2019. An automated Raman-based platform for the sorting of live cells by functional properties. Nat Microbiol 4:1035–1048. https://doi.org/10.1038/s41564-019-0394-9.
13. Lee KS, Wagner M, Stocker R. 2020. Raman-based sorting of microbial cells to link functions to their genes. Microb Cell 7:62–65. https://doi.org/10.15698/mic2020.03.709.
14. Stryhanyuk H, Calabrese F, Kümmel S, Musat F, Richnow HH, Musat N. 2018. Calculation of single cell assimilation rates from SIP-NanoSIMS-derived isotope ratios: a comprehensive approach. Front Microbiol 9: 2342. https://doi.org/10.3389/fmicb.2018.02342.
15. Musat N, Halm H, Winterholler B, Hoppe P, Peduzzi S, Hillion F, Horreard F, Amann R, Jørgensen BB, Kuypers MMM. 2008. A single-cell view on the ecophysiology of anaerobic phototrophic bacteria. Proc Natl Acad Sci U S A 105:17861–17866. https://doi.org/10.1073/pnas.0809329105.
16. Ellis DI, Cowcher DP, Ashton L, O'Hagan S, Goodacre R. 2013. Illuminating disease and enlightening biomedicine: Raman spectroscopy as a diagnostic tool. Analyst 138:3871–3884. https://doi.org/10.1039/c3an00698k.
17. Butler HJ, Ashton L, Bird B, Cinque G, Curtis K, Dorney J, Esmonde-White K, Fullwood NJ, Gardner B, Martin-Hirsch PL, Walsh MJ, McAinsh MR, Stone N, Martin FL. 2016. Using Raman spectroscopy to characterize biological materials. Nat Protoc 11:664–687. https://doi.org/10.1038/nprot.2016.036.
18. Palonpon AF, Sodeoka M, Fujita K. 2013. Molecular imaging of live cells by Raman microscopy. Curr Opin Chem Biol 17:708–715. https://doi.org/10.1016/j.cbpa.2013.05.021.
19. Palonpon AF, Ando J, Yamakoshi H, Dodo K, Sodeoka M, Kawata S, Fujita K. 2013. Raman and SERS microscopy for molecular imaging of live cells. Nat Protoc 8:677–692. https://doi.org/10.1038/nprot.2013.030.
20. Noothalapati Venkata HN, Shigeto S. 2012. Stable isotope-labeled Raman imaging reveals dynamic proteome localization to lipid droplets in single fission yeast cells. Chem Biol 19:1373–1380. https://doi.org/10.1016/j.chembiol.2012.08.020.
21. Noothalapati H, Shigeto S. 2014. Exploring metabolic pathways in vivo by a combined approach of mixed stable isotope-labeled Raman microspectroscopy and multivariate curve resolution analysis. Anal Chem 86:7828–7834. https://doi.org/10.1021/ac501735c.
22. Yakubovskaya E, Zaliznyak T, Martínez Martínez J, Taylor GT. 2019. Tear down the fluorescent curtain: a new fluorescence suppression method for Raman microspectroscopic analyses. Sci Rep 9:15785. https://doi.org/10.1038/s41598-019-52321-3.
23. Huang WE, Griffiths RI, Thompson IP, Bailey MJ, Whiteley AS. 2004. Raman microscopic analysis of single microbial cells. Anal Chem 76:4452–4458. https://doi.org/10.1021/ac049753k.
24. Wang Y, Huang WE, Cui L, Wagner M. 2016. Single cell stable isotope probing in microbiology using Raman microspectroscopy. Curr Opin Biotechnol 41:34–42. https://doi.org/10.1016/j.copbio.2016.04.018.
25. Taylor GT, Suter EA, Li ZQ, Chow S, Stinton D, Zaliznyak T, Beaupré SR. 2017. Single-cell growth rates in photoautotrophic populations measured by stable isotope probing and resonance Raman microspectrometry. Front Microbiol 8:1449. https://doi.org/10.3389/fmicb.2017.01449.
26. Muhamadali H, Chisanga M, Subaihi A, Goodacre R. 2015. Combining Raman and FT-IR spectroscopy with quantitative isotopic labeling for differentiation of E. coli cells at community and single cell levels. Anal Chem 87:4578–4586. https://doi.org/10.1021/acs.analchem.5b00892.
27. Kumar VBN, Guo S, Bocklitz T, Rösch P, Popp J. 2016. Demonstration of carbon catabolite repression in naphthalene degrading soil bacteria via Raman spectroscopy based stable isotope probing. Anal Chem 88:7574–7582. https://doi.org/10.1021/acs.analchem.6b01046.
28. Huang WE, Stoecker K, Griffiths R, Newbold L, Daims H, Whiteley AS, Wagner M. 2007. Raman-FISH: combining stable-isotope Raman spectroscopy and fluorescence in situ hybridization for the single cell analysis of identity and function. Environ Microbiol 9:1878–1889. https://doi.org/10.1111/j.1462-2920.2007.01352.x.
29. Grossart HP, Massana R, McMahon KD, Walsh DA. 2020. Linking metagenomics to aquatic microbial ecology and biogeochemical cycles. Limnol Oceanogr 65:S2–S20. https://doi.org/10.1002/lno.11382.
30. Singer E, Wagner M, Woyke T. 2017. Capturing the genetic makeup of the active microbiome in situ. ISME J 11:1949–1963. https://doi.org/10.1038/ismej.2017.59.
31. Huang WE, Ferguson A, Singer AC, Lawson K, Thompson IP, Kalin RM, Larkin MJ, Bailey MJ, Whiteley AS. 2009. Resolving genetic functions within microbial populations: in situ analyses using rRNA and mRNA stable isotope probing coupled with single-cell Raman-fluorescence in situ hybridization. Appl Environ Microbiol 75:234–241. https://doi.org/10.1128/AEM.01861-08.
32. Movasaghi Z, Rehman S, Rehman IU. 2007. Raman spectroscopy of biological tissues. Appl Spectrosc Rev 42:493–541. https://doi.org/10.1080/05704920701551530.
33. Zhu G, Zhu X, Fan Q, Wan X. 2011. Raman spectra of amino acids and their aqueous solutions. Spectrochim Acta A Mol Biomol Spectrosc 78: 1187–1195. https://doi.org/10.1016/j.saa.2010.12.079.
34. Czamara K, Majzner K, Pacia MZ, Kochan K, Kaczor A, Baranska M. 2015. Raman spectroscopy of lipids: a review. J Raman Spectrosc 46:4–20. https://doi.org/10.1002/jrs.4607.
35. De Gelder J, De Gussem K, Vandenabeele P, Moens L. 2007. Reference database of Raman spectra of biological molecules. J Raman Spectrosc 38:1133–1147. https://doi.org/10.1002/jrs.1734.
36. Elso CM, Roberts LJ, Smyth GK, Thomson RJ, Baldwin TM, Foote SJ, Handman E. 2004. Leishmaniasis host response loci (lmr1-3) modify disease severity through a Th1/Th2-independent pathway. Genes Immun 5: 93–100. https://doi.org/10.1038/sj.gene.6364042.
37. Lin HL, Lin CC, Lin YJ, Lin HC, Shih CM, Chen CR, Huang RN, Kuo TC. 2010. Revisiting with a relative-density calibration approach the determination of growth rates of microorganisms by use of optical density data from

liquid cultures. Appl Environ Microbiol 76:1683–1685. https://doi.org/10.1128/AEM.00824-09.

38. Myers JA, Curtis BS, Curtis WR. 2013. Improving accuracy of cell and chromophore concentration measurements using optical density. BMC Biophys 6:4. https://doi.org/10.1186/2046-1682-6-4.
39. Bland JM, Altman DG. 1986. Statistical methods for assessing agreement between two methods of clinical measurement. Lancet i:307–310.
40. Li M, Huang WE, Gibson CM, Fowler PW, Jousset A. 2013. Stable isotope probing and Raman spectroscopy for monitoring carbon flow in a food chain and revealing metabolic pathway. Anal Chem 85:1642–1649. https://doi.org/10.1021/ac302910x.
41. Lorenz B, Wichmann C, Stöckel S, Rösch P, Popp J. 2017. Cultivation-free Raman spectroscopic investigations of bacteria. Trends Microbiol 25:413–424. https://doi.org/10.1016/j.tim.2017.01.002.
42. Xie C, Mace J, Dinno MA, Li YQ, Tang W, Newton RJ, Gemperline PJ. 2005. Identification of single bacterial cells in aqueous solution using confocal laser tweezers Raman spectroscopy. Anal Chem 77:4390–4397. https://doi.org/10.1021/ac0504971.
43. Huang WE, Bailey MJ, Thompson IP, Whiteley AS, Spiers AJ. 2007. Single-cell Raman spectral profiles of Pseudomonas fluorescens SBW25 reflects in vitro and in planta metabolic history. Microb Ecol 53:414–425. https://doi.org/10.1007/s00248-006-9138-5.
44. Huang WE, Ward AD, Whiteley AS. 2009. Raman tweezers sorting of single microbial cells. Environ Microbiol Rep 1:44–49. https://doi.org/10.1111/j.1758-2229.2008.00002.x.
45. Huang WE, Li M, Jarvis RM, Goodacre R, Banwart SA. 2010. Shining light on the microbial world: the application of Raman microspectroscopy. Adv Appl Microbiol 70:153–186. https://doi.org/10.1016/S0065-2164(10)70005-8.
46. Cui L, Yang K, Zhou G, Huang WE, Zhu Y-G. 2017. Surface-enhanced Raman spectroscopy combined with stable isotope probing to monitor nitrogen assimilation at both bulk and single-cell level. Anal Chem 89:5793–5800. https://doi.org/10.1021/acs.analchem.6b04913.
47. Wang Y, Song Y, Zhu D, Ji Y, Wang T, McIlvenna D, Yin H, Xu J, Huang WE. 2013. Probing and sorting single cells: the application of a Raman-activated cell sorter. Spectrosc Eur 25:16–20.
48. Kubryk P, Kölschbach JS, Marozava S, Lueders T, Meckenstock RU, Niessner R, Ivleva NP. 2015. Exploring the potential of stable isotope (resonance) Raman microspectroscopy and surface-enhanced Raman scattering for the analysis of microorganisms at single cell level. Anal Chem 87:6622–6630. https://doi.org/10.1021/acs.analchem.5b00673.
49. Eichorst SA, Strasser F, Woyke T, Schintlmeister A, Wagner M, Woebken D. 2015. Advancements in the application of NanoSIMS and Raman microspectroscopy to investigate the activity of microbial cells in soils. FEMS Microbiol Ecol 91:fiv106. https://doi.org/10.1093/femsec/fiv106.
50. Haider S, Wagner M, Schmid MC, Sixt BS, Christian JG, Häcker G, Pichler P, Mechtler K, Müller A, Baranyi C, Toenshoff ER, Montanaro J, Horn M. 2010. Raman microspectroscopy reveals long-term extracellular activity of chlamydiae. Mol Microbiol 77:687–700. https://doi.org/10.1111/j.1365-2958.2010.07241.x.
51. Braun A, Spona-Friedl M, Avramov M, Elsner M, Baltar F, Reinthaler T, Herndl GJ, Griebler C. 2021. Reviews and syntheses: heterotrophic fixation of inorganic carbon—significant but invisible flux in environmental carbon cycling. Biogeosciences 18:3689–3700. https://doi.org/10.5194/bg-18-3689-2021.
52. Gibson F, Pittard J. 1968. Pathways of biosynthesis of aromatic amino acids and vitamins and their control in microorganisms. Bacteriol Rev 32:465–492. https://doi.org/10.1128/br.32.4_pt_2.465-492.1968.
53. Spona-Friedl M, Braun A, Huber C, Eisenreich W, Griebler C, Kappler A, Elsner M. 2020. Substrate-dependent CO2 fixation in heterotrophic bacteria revealed by stable isotope labelling. FEMS Microbiol Ecol 96:fiaa080. https://doi.org/10.1093/femsec/fiaa080.
54. Blair N, Leu A, Muñoz E, Olsen J, Kwong E, Des Marais D. 1985. Carbon isotopic fractionation in heterotrophic microbial metabolism. Appl Environ Microbiol 50:996–1001. https://doi.org/10.1128/aem.50.4.996-1001.1985.
55. Macko SA, Estep MLF. 1984. Microbial alteration of stable nitrogen and carbon isotopic compositions of organic matter. Org Geochem 6:787–790. https://doi.org/10.1016/0146-6380(84)90100-1.
56. Monson KD, Hayes JM. 1980. Biosynthetic control of the natural abundance of carbon 13 at specific positions within fatty acids in Escherichia coli. Evidence regarding the coupling of fatty acid and phospholipid synthesis. J Biol Chem 255:11435–11441. https://doi.org/10.1016/S0021-9258(19)70310-X.
57. Hullar MAJ, Fry B, Peterson BJ, Wright RT. 1996. Microbial utilization of estuarine dissolved organic carbon: a stable isotope tracer approach tested by mass balance. Appl Environ Microbiol 62:2489–2493. https://doi.org/10.1128/aem.62.7.2489-2493.1996.
58. Fang J, Lovanh N, Alvarez PJJ. 2004. The use of isotopic and lipid analysis techniques linking toluene degradation to specific microorganisms: applications and limitations. Water Res 38:2529–2536. https://doi.org/10.1016/j.watres.2004.03.006.
59. Kirchman DL. 1993. Leucine incorporation as a measure of biomass production by heterotrophic bacteria, p 509–512. *In* Kemp PF, Sherr BF, Sherr EB, Cole JJ (ed), Handbook of methods in aquatic microbial ecology, 1st ed. CRC Press, Boca Raton, FL.
60. Fuhrman JA, Azam F. 1982. Thymidine incorporation as a measure of heterotrophic bacterioplankton production in marine surface waters: evaluation and field results. Mar Biol 66:109–120. https://doi.org/10.1007/BF00397184.
61. Vogt C, Lueders T, Richnow HH, Krüger M, Von Bergen M, Seifert J. 2016. Stable isotope probing approaches to study anaerobic hydrocarbon degradation and degraders. J Mol Microbiol Biotechnol 26:195–210. https://doi.org/10.1159/000440806.
62. Radajewski S, Ineson P, Parekh NR, Murrell JC. 2000. Stable-isotope probing as a tool in microbial ecology. Nature 403:646–649. https://doi.org/10.1038/35001054.
63. Radajewski S, McDonald IR, Murrell JC. 2003. Stable-isotope probing of nucleic acids: a window to the function of uncultured microorganisms. Curr Opin Biotechnol 14:296–302. https://doi.org/10.1016/s0958-1669(03)00064-8.
64. Manefield M, Whiteley AS, Griffiths RI, Bailey MJ. 2002. RNA stable isotope probing, a novel means of linking microbial community function to phylogeny. Appl Environ Microbiol 68:5367–5373. https://doi.org/10.1128/AEM.68.11.5367-5373.2002.
65. Kubryk P, Niessner R, Ivleva NP. 2016. The origin of the band at around 730 cm−1 in the SERS spectra of bacteria: a stable isotope approach. Analyst 141:2874–2878. https://doi.org/10.1039/c6an00306k.
66. Sharp JH. 1974. Improved analysis for "particulate" organic carbon and nitrogen from seawater. Limnol Oceanogr 19:984–989. https://doi.org/10.4319/lo.1974.19.6.0984.
67. Taylor GT, Li Z-Q, Suter E, Chow S. 2017. Modified filter-transfer-freeze ("FTF") technique for Raman microspectroscopic analysis of single cells. protocols.io https://doi.org/10.17504/protocols.io.ikqccvw.
68. Soper DS. 2021. Significance of the difference between two slopes calculator. https://www.danielsoper.com/statcalc.

Supplemental Materials for:

Using Stable Isotope Probing and Raman Microspectroscopy to measure growth rates of heterotrophic bacteria

Felix Weber, Tatiana Zaliznyak, Virginia P. Edgcomb, Gordon T. Taylor

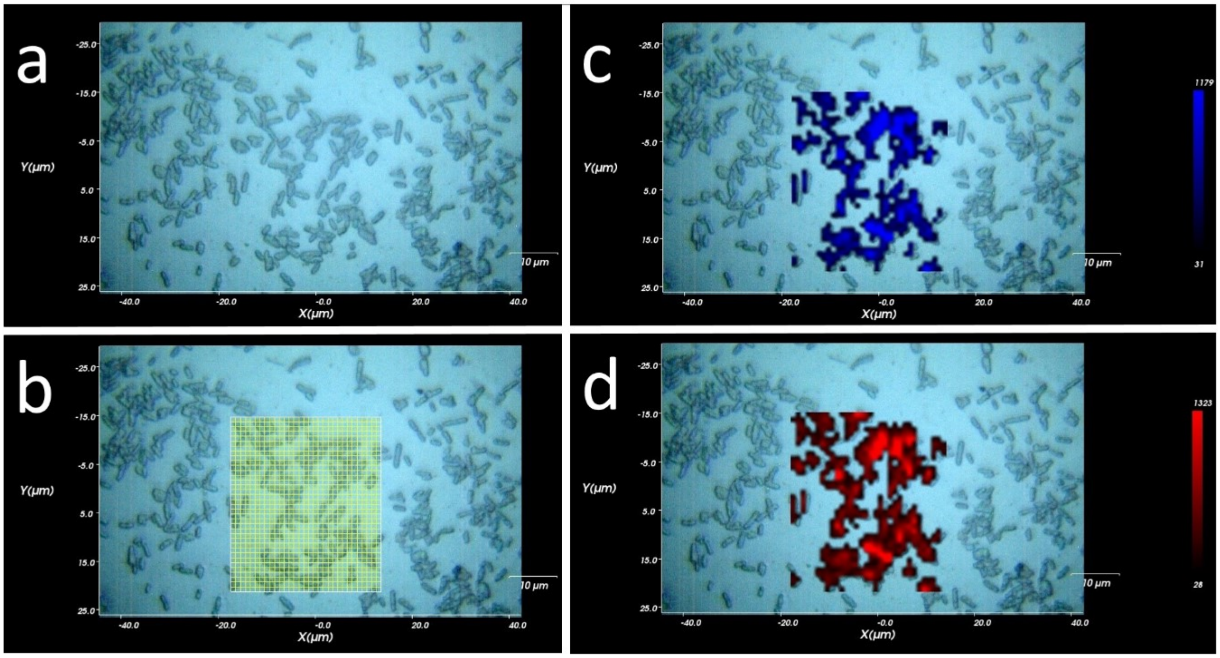

Figure S1. Illustration of Raman mapping procedure of a cluster of *E.coli* Bs-1 cells after growth (88 min) in ^{13}C-labeled Bioexpress® medium (f_{media} = 0.348). Cell cluster micrograph (InVia camera) at a magnification of 1000x (a). Mapping grid overlay with 1184 nodes covering 114 *E.coli* Bs-1 cells (b). Mapping result after a 6 h Raman scan (exposure = 18 sec per node) showing peak height intensity at 1002 cm^{-1} and 966 cm^{-1} in panels (c) and (d), respectively.

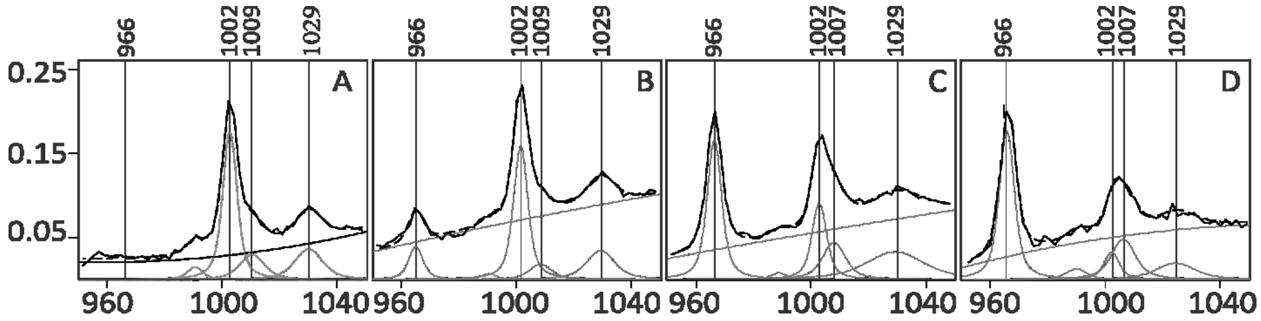

Figure S2. Illustration of curve-fitting procedure to quantify peak intensities of the two dominant phenylalanine isotopologues at select time points during the incubation in ^{13}C-labeled Bioexpress® medium ($f_{\mathrm{media}} = 0.985$). Panels A-D show results after 0, 30, 88 and 180 min of incubation with average f_{cell} values of 0.02, 0.19, 0.68 and 0.89, respectively. Solid and dashed black lines represent averaged spectra and sum of the fitted peaks, respectively. Underlying diagonal line is the baseline correction. Individual fitted peaks at wavenumbers 966, 1002, 1007, 1009, 1029 cm^{-1} are indicated by the gray vertical lines. Peaks at wavenumbers 966 and 1002 cm^{-1} correspond to the Phe "ring breathing mode" of the fully labeled and natural abundance aromatic rings, respectively.

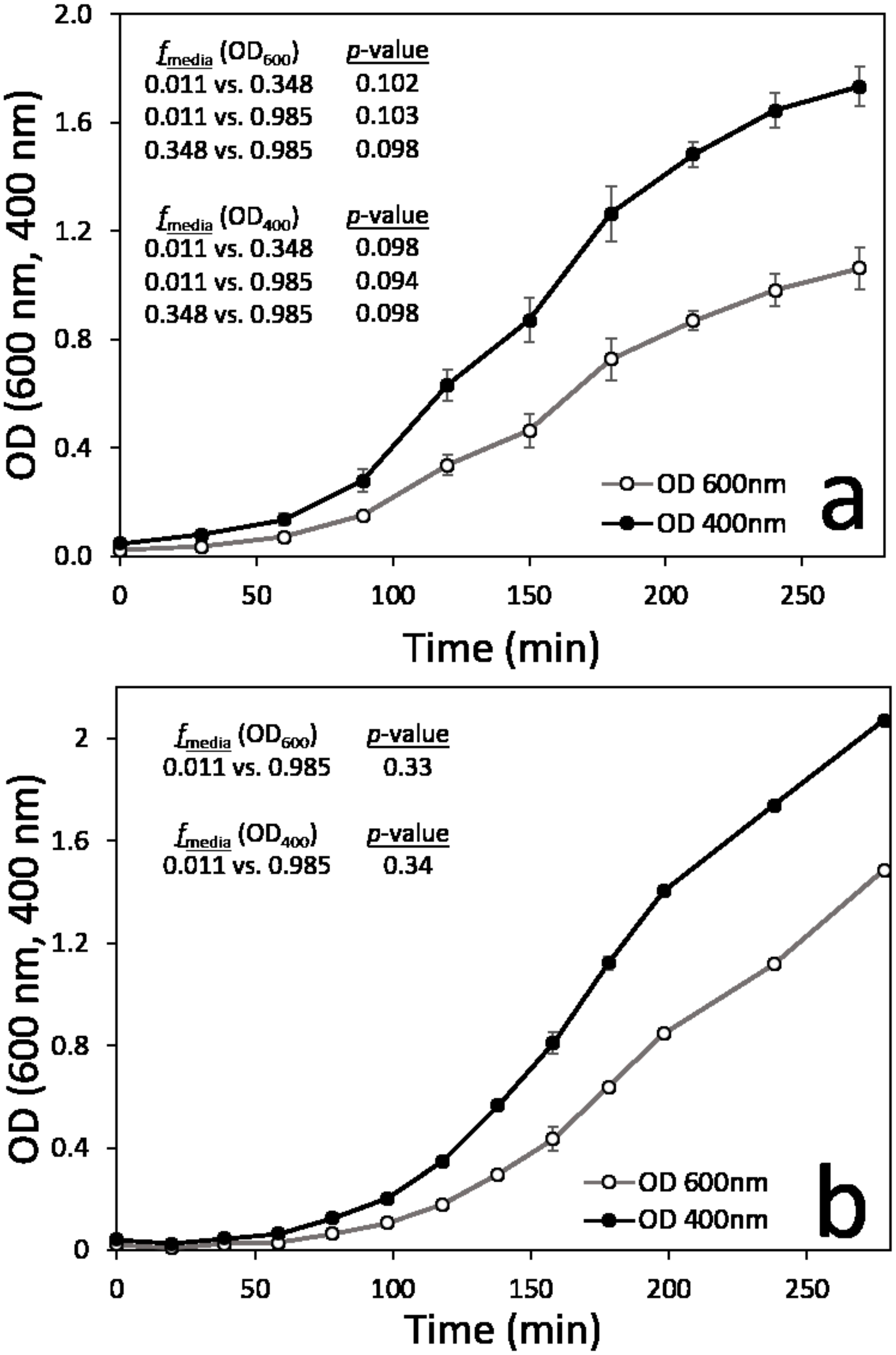

Figure S3. Growth curves of *E. coli* Bs-1 (a) and *E. coli* K (b) grown in three (f_{media} = 0.011, 0.348 and 0.985) and two (f_{media} = 0.011 and 0.985) labeling treatments, respectively. Mean (± 1 SD) OD-values at 600 and 400 nm are based on nine (sample triplicates of three treatments) and four (sample duplicates of two treatments) OD measurements in (a) and (b), respectively. In most cases, ±1 SD was smaller than the symbol. Statistical comparison of growth curves found no significant difference ($p\text{-value} > 0.05$) among labeling treatments (f_{media}). Pairwise comparison of labeling treatments was performed by a statistical permutation test (10000 iterations) (68). Respective p-values are given in each panel.